Research Square

Preprints are preliminary reports that have not undergone peer review.
They should not be considered conclusive, used to inform clinical practice,
or referenced by the media as validated information.

3D shear-wave velocity model of the crust underneath Llaima volcano, Chile

J. Augusto Casas

augusto.casas@segemar.gob.ar

Servicio Geológico Minero Argentino, CONICET

Damián Inghilterra

Universidad Nacional de La Plata

Gabriela Badi

Universidad Nacional de La Plata

Luis Franco-Marín

Servicio Nacional de Geologia y Mineria

T. Dylan Mikesell

Norwegian Geotechnical Institute

Deyan Draganov

Delft University of Technology

Research Article

Keywords:

Posted Date: November 26th, 2026

DOI: https://doi.org/10.21203/rs.3.rs-11526570/v1

License: This work is licensed under a Creative Commons Attribution 4.0 International License.
Read Full License

Additional Declarations: No competing interests reported.

3D shear-wave velocity model of the crust underneath Llaima volcano, Chile

J. Augusto Casas[a,b,*], Damián Inghilterra[b], Gabriela Badi[b], Luis Franco-Marín[c], T. Dylan Mikesell[d], Deyan Draganov[e]

Affiliations

[a] Observatorio Argentino de Vigilancia Volcánica (OAVV), Servicio Geológico Minero Argentino, CONICET, Buenos Aires, Argentina

[b] Centro de Investigaciones Geofísicas (CIGEOF), Universidad Nacional de La Plata, La Plata, Argentina

[c] Observatorio Vulcanológico de los Andes del Sur, Servicio Nacional de Geología y Minería, Temuco, Chile

[d] Norwegian Geotechnical Institute, Oslo, Norway

[e] Department of Geoscience and Engineering, Delft University of Technology, Delft, The Netherlands

ORCID

J. Augusto Casas	0000-0002-6190-157X
Damián Inghilterra	0009-0005-8602-2394
Gabriela Badi	0000-0003-0512-1015
Luis Franco-Marín	0000-0001-7112-7277
T. Dylan Mikesell	0000-0001-9900-9846
Deyan Draganov	0000-0001-8606-1178

Corresponding author

*J. Augusto Casas, E-mail: **augusto.casas@segemar.gob.ar**

3D shear-wave velocity model of the crust underneath Llaima volcano, Chile

J. Augusto Casas, Damián Inghilterra, Gabriela Badi, Luis Franco-Marín, T. Dylan Mikesell, Deyan Draganov

Abstract

Llaima volcano, an active stratovolcano in the Southern Andes, has experienced recurrent explosive eruptions that reflect a complex and dynamic magmatic system. Its most recent eruptions, characterized by ash columns exceeding 10 km in height, underscore the need for a better understanding of this volcanic system, particularly through improved constraints on its subsurface structure and magmatic plumbing architecture. Although previous studies have provided insights into the subsurface structure of Llaima, the geometry and depth of its magma reservoirs remain debated. To address these uncertainties, we image the subsurface beneath Llaima using seismic tomography based on ambient-noise interferometry. We analyze seismic records from 49 stations of three contemporaneous seismic networks deployed around the volcano to derive a three-dimensional shear-wave velocity model extending to 18 km depth beneath the surface. Our model provides the first comprehensive 3-D characterization of Llaima's crustal structure at these depth and spatial scales. Our results reveal pronounced lateral and vertical heterogeneity, offering new constraints on the volcano's magmatic architecture

and supporting a vertically segmented plumbing system, consisting of shallow magma storage down to 4 km depth, a deeper magma source between 10 and 18 km depth, and an intermediate transition zone separating these levels.
Keywords: Ambient seismic noise, Rayleigh-wave phase velocity maps, Llaima volcano, Subsurface volcano structure, Magma reservoirs

1. Introduction

Llaima volcano (38°41.9'S, 71°43.8'W) is a basaltic-andesitic stratovolcano located in the Southern Volcanic Zone in Chile, approximately 285 km East of the subduction trench (Stern, 2004) (Fig. 1). The summit crater of Llaima volcano is approximately 350 m in diameter and is associated with a coalescent cone whose summit lies about 1 km to the SSE of the crater. The latter was the vent for the significant effusive activity during the 1957 eruption (Naranjo and Moreno, 1991). The composite edifice has a volume of approximately 380 km^3 and covers an area of 440 km^2 (Völker et al., 2011). Llaima has around 40 satellite scoria cones located at the NE, NW and SW flanks of the volcano, which are associated to the subsurface emplacement of magma (Schonwalder-Angel et al., 2018). Several flank vents are distributed along a NE-SW trending direction, a feature regionally observed in the Southern Andes Volcanic Zone and interpreted as indicator of the intra-arc stress regime (Cembrano and Lara, 2009).

This active volcano has experienced explosive eruptions (Volcanic Ex-

plosivity Index -VEI≤4) during the last 400 years (González-Ferrán, 1995; Petit-Breuilh Sepúlveda, 2018), posing a threat to the population of approximately 20,000 people living within a radius of 30 km from the volcano (Global Volcanism Program, 2026). According to its eruptive history and the population located in its surroundings, this active volcano ranks second in the Hazards Volcanic Ranking for Chile (Lara et al., 2021). Despite the risk imposed by Llaima, the number of published articles providing evidence about its subsurface structure and dynamics is low compared to other volcanoes in the Southern Volcanic Zone (Romero et al., 2024). In particular, the geometry of Llaima's magmatic system is still poorly constrained.

The close location of both the Liquiñe-Ofqui Fault System and the Andean Transversal Faults to Llaima volcano has strongly determined its subsurface structures and conditions (Romero et al., 2024). During the last 3,000 years, magma storage depths changed from middle crust to upper crust as a consequence of a change in the tectonic regime from transpression to tension. The depth variation of the magma accumulation zones resulted in a change of the eruptive style and the frequency of the eruptions, as a consequence of both assimilation of granitic rocks from the host rock and an increased saturation of water at these depths (Schindlbeck et al., 2014).

Llaima volcano presents a high eruptive frequency; statistical analyses indicate a ≥90% probability of an eruption with VEI≥2 within 20 years after its most recent eruption in 2009 (Dzierma and Wehrmann, 2010). However, the volcanic activity at Llaima changed in response to local and regional stress

variations produced by the 2010 Mw 8.8 Maule earthquake. Long-period and tremor seismic events, typically caused by fluid flow and resonance of cracks (Wassermann, 2012), significantly reduced in number and energy levels while maintaining their location along NW-SE trend crossing the volcanic edifice for 2009-2013; Franco-Marín et al. (2023) interpreted this feature as evidence of magma motion towards the main crater.

At crustal depths, a few studies were performed with the aim to estimate the location of the subsurface magma-accumulation volumes. Based on receiver-function analysis applied to earthquake seismic data, Bishop et al. (2018) provided evidence for a subsurface volume characterized by low seismic velocities, interpreted as a magma body located mainly to the SE of the main crater and at depths of 10–15 km. Through geochemical analyses, De Maisonneuve et al. (2012a) and Ruth et al. (2016) proposed that a crystal mush is originated at 1-4 km depth as a consequence of crystallization processes after quasi-constant degassing and, therefore, an increase of the viscosity of the material emplaced at these depths. Violent eruptions at Llaima are attributed to repeated magma injections from deeper source regions, estimated to lie below 10 km depth, into shallow feeder and magma accumulation zones. The associated volatile input modifies the physical properties of the crystal mush, facilitating the rapid ascent of gases toward the surface (De Maisonneuve et al., 2012b).

Despite these advances, key aspects of Llaima's magmatic system remain unresolved. In particular, the geometry, depth distribution, and connectivity

of magma-accumulation zones within the crust are still debated. It is unclear whether magma storage is organized as a vertically layered system, a laterally segmented structure, or a combination of both, and how shallow and deep reservoirs interact. Resolving these issues is critical for constraining the architecture of the magmatic plumbing system and its role in controlling eruptive dynamics.

2. Data

We use seismic data recorded by three seismic networks (coded as TC, XW and 3H, the latter two available in the IRIS databases) totaling 49 stations recording at 100 samples per second for ambient seismic noise tomography (see station distribution in Fig. 1). The network XW (Mikesell, 2015) was temporarily deployed between January and March 2015 after a coordinated effort from Boise State University (United States), University of North Carolina at Chapel Hill (United States) and OVDAS-SERNAGEOMIN (Chile). The XW stations were installed within a 20×25 km^2 area surrounding Llaima volcano and all of the stations were equipped with a variety of 3-component broadband seismometers (Supplementary Material, Table S1). The TC network is composed of stations used by OVDAS-SERNAGEOMIN for real-time monitoring; this network includes eight seismic stations equipped with 3-component broadband seismometers (Supplementary Material, Table S2). The 3H network was deployed as part of the SAIAS experiment (Lange et al., 2019). The stations in this network were equipped with 3-component

broadband and short-period (1 Hz) seismometers (Supplementary Material, Table S3). Previous studies have demonstrated reliable ambient-noise measurements with these 1-Hz seismometers down to 0.1 Hz following instrument-response correction (Strollo et al., 2008).

3. Methods and Reliability tests

3.1. Pre-processing and phase velocities measurements

We pre-process the seismograms recorded by the XW, TC and 3H networks; we apply a low-pass anti-alias filter at 5 Hz, decimate the seismograms to 10 samples per second, demean, detrend and taper. For the removal of the instrument response, we first build the corresponding instrument response function for all the stations using the information provided by the institutions that installed the networks. We converted the resulting waveforms from every station to displacement.

We used these pre-processed seismic data to obtain ambient-noise phase velocities using the SeisLib library (Magrini et al., 2022). Considering the three available networks, receiver pairs with at least one month of simultaneous recordings are selected (see raypaths in Fig. 2a). For each pair, seismograms are cross-correlated using 1-hour-long windows with 50% overlap, and the resulting correlation functions are linearly stacked to enhance the signal-to-noise ratio.

The spectrum of the obtained correlation approximates the zeroth-order Bessel function of the first kind $J_0\left(\frac{\omega\Delta}{c(\omega)}\right)$, where Δ denotes inter-station

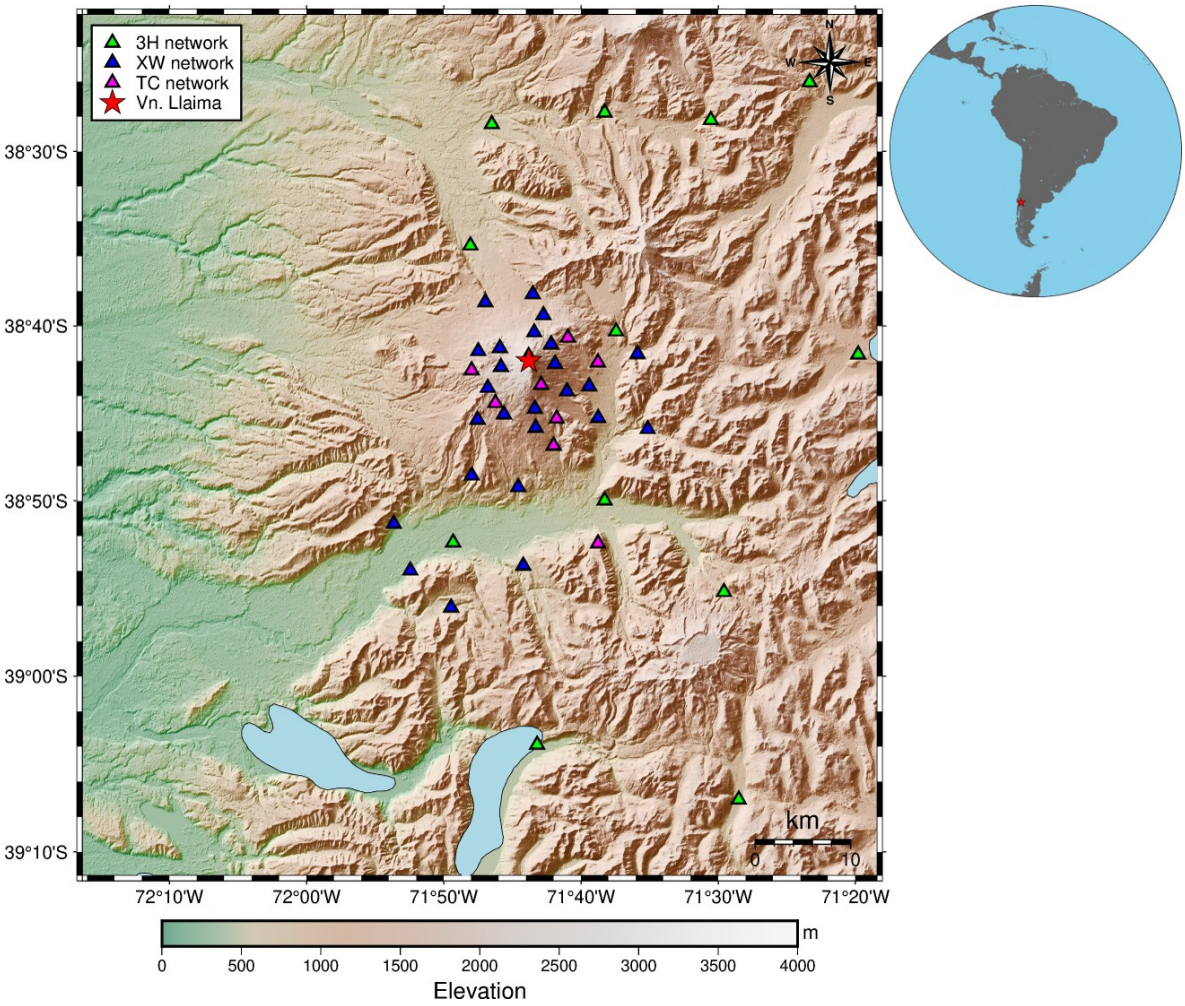

Fig. 1 Topographical map showing the location of Llaima volcano (red star) and the used seismic stations (triangles). Triangles with different colors refer to different seismic networks. The inset on the upper right corner indicates the location of the study area in South America

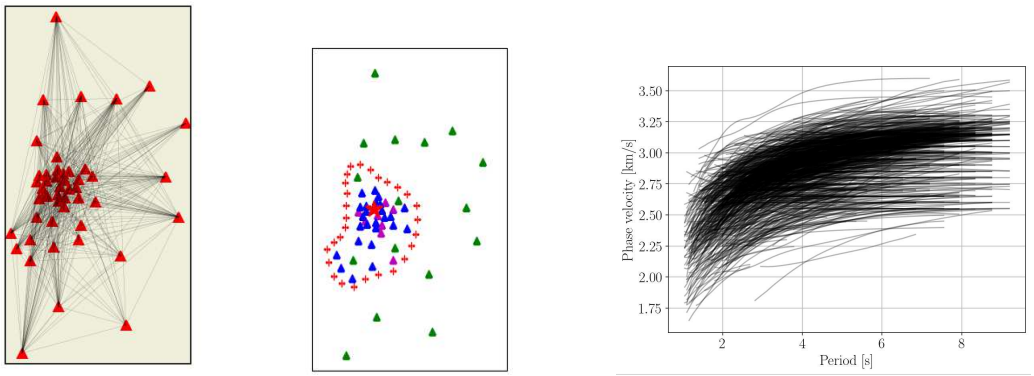

(a) **(b)** **(c)**

Fig. 2 (a) Ray paths (gray lines) between stations (red triangles) with simultaneous records for at least one month. (b) Area with a higher density of rays selected for processing (bounded by red cross markers); triangles represent seismic stations. (c) Resulting Rayleigh-wave phase-velocity dispersion curves

distance. Thus, we obtain phase-velocity values c as a function of angular frequency ω using vertical-component data through an automated algorithm (Magrini et al., 2022). Provided several velocity values are obtained for each frequency, a reference curve, which we obtain from a regional velocity model (Ekström et al., 1997), is used to solve for the phase-velocity ambiguity at low frequencies (i.e., periods higher than 5 s); then, velocity values for higher frequencies are automatically selected based on a smooth extrapolation. We obtain 810 Rayleigh-wave dispersion curves (Fig. 2c), for periods between 1 and 10 s. These period bounds result from the interstation distance and the frequency interval within which the coherency of the surface-wave energy is maximum for each station pair.

For each pair of receivers, we assume that the dispersion curve contains information of the propagation of surface waves along the great-circle path

connecting the stations. We invert the dispersion curves to analyze the spatial variations of the phase velocity using a linearized least-squares inversion algorithm based on ray theory (Magrini et al., 2022). The spatial parameterization is adapted to ray density. For each period considered in the inversion, an initial coarse grid with a cell size of $0.1^\circ \times 0.1^\circ$ is used. Grid cells intersected by more than 100 ray paths are recursively subdivided into four subcells. This adaptive refinement aims to improve the spatial allocation of the information carried by the rays, thereby increasing the effective resolution of the model. Once refined, the subdivision is not reversed, even if some of the resulting subcells are intersected by few or no ray paths. This procedure is repeated up to two times, resulting in a minimum cell size of $0.025^\circ \times 0.025^\circ$.

To regularize the inversion, we apply a roughness–damping criterion, whereby an optimal roughness parameter is determined for each period through L-curve analysis (Hansen, 1999). Then, roughness values range from 2.4×10^{-4} to 3.7×10^{-4}. As an example, Fig. 3 shows the Rayleigh-wave phase-velocity maps obtained for periods of 3 s and 5 s.

3.2. Reliability of the tomographic results

We perform checkerboard tests to evaluate the spatial resolution of the retrieved phase-velocity variations. For each period considered in the inversion of the field data, and using the same station distribution, we generate synthetic velocity anomalies following a predefined checkerboard pattern with

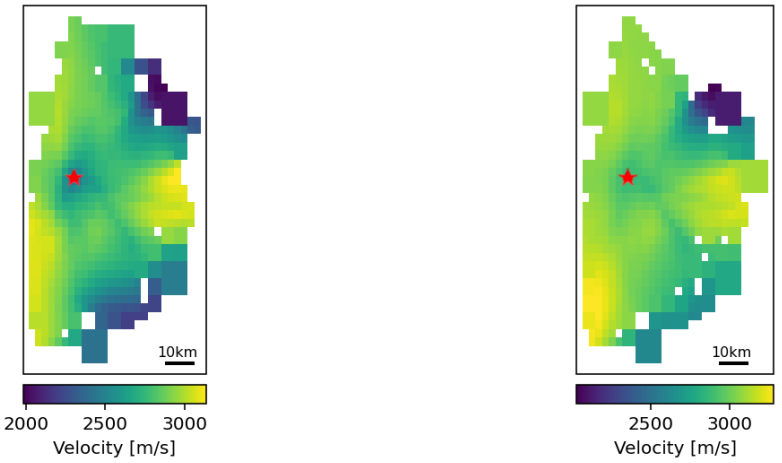

Fig. 3 Rayleigh-wave velocity maps for periods (a) 3 s and (b) 5 s. The red star indicates the location of Llaima volcano

the finest cell refinement adopted for that period (Fig. 4). These anomalies are then used to compute synthetic interstation phase-velocity dispersion curves. These synthetic curves are inverted using the same methodology applied to the field data, and the recovered models are compared with the input synthetic models. The results indicate that phase velocities are reliably retrieved within the area characterized by the highest ray-path density (Fig. 2b). Note that, although the analysis is restricted to the selected area, all available ray paths are considered, including those connecting station pairs with stations located outside this area. At the surface, this region encompasses the Llaima volcanic edifice and covers an area of 689 km^2.

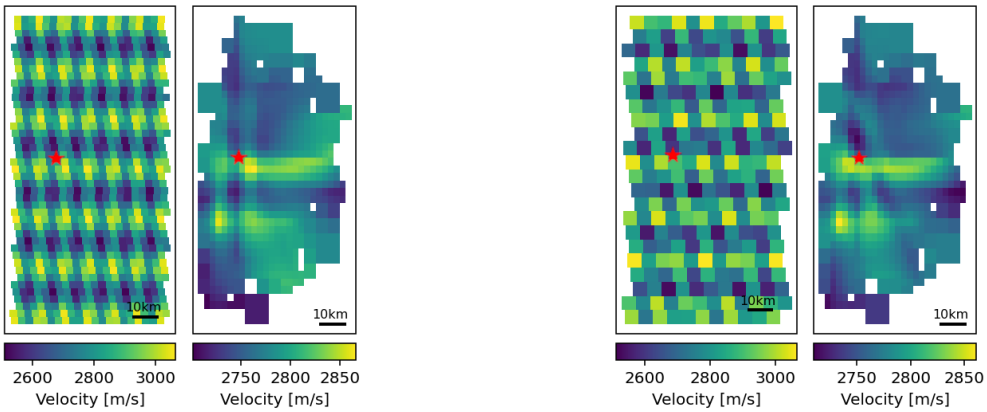

(a) **(b)**

Fig. 4 Comparison between the synthetic model (left) and the retrieved model (right) from checkerboard tests using different cell sizes for different periods (T). (a) A cell size of 0.05° for T=7 s, and (b) a cell size of 0.025° for T=4 s

3.3. Sensitivity kernels

The vertical coordinate of our tomographic model is referenced to the mean elevation of the seismic stations (i.e., 1.24 km above the sea level). Throughout the manuscript, depths are therefore reported relative to this reference elevation and are referred to as depths below the surface for simplicity.

To assess the depth sensitivity of the inversion, we use an isotropic elastic Earth model composed of homogeneous layers, which corresponds to the model employed by OVDAS for daily monitoring purposes. We then compute multi-modal surface-wave dispersion curves and eigenfunctions, from which sensitivity kernels of Rayleigh-wave phase velocity with respect to S-wave velocity are derived for the frequency range used in the inversion (Zhang, 2018). Fig. 5 shows the resulting kernels for periods common to all station

pairs (i.e., 2–6 s). The sensitivity kernels exhibit a Gaussian-like shape, characterized by a local minimum at shallow depths. For each kernel, we define the depth sensitivity range as the interval over which the sensitivity exceeds this local minimum value. The results indicate that our model is sensitive to depths between 0.5 and 18 km.

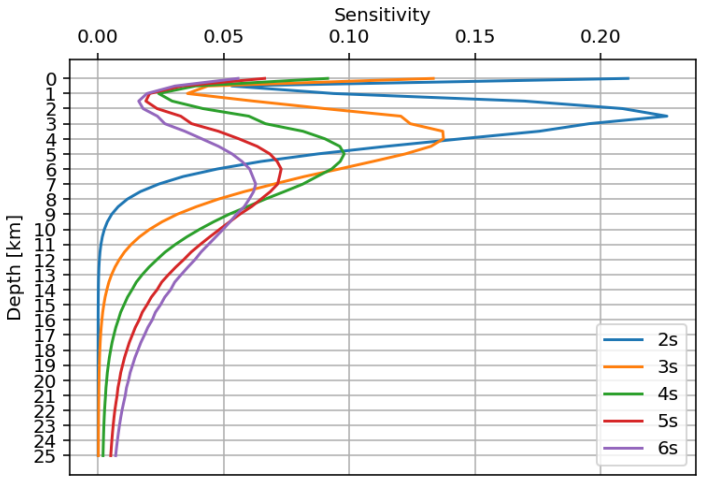

Fig. 5 Sensitivity kernels of the Rayleigh-wave fundamental mode

4. S-wave velocity model

We use the phase-velocity maps to obtain a 3D shear-wave velocity model for the subsurface underneath Llaima volcano. For each inverted period, the overall minimum cell size adopted in the phase-velocity maps ($0.025° \times 0.025°$) is used to interpolate Rayleigh-wave velocities. This procedure yielded a dispersion curve at each grid cell, which we subsequently nonlinearly inverted to estimate the S-wave velocity structure as a function of depth. The resulting

1D models are then spatially combined using the Bayesian inversion framework BayHunter (Dreiling and Tilmann, 2019) to construct a 3D S-wave velocity model for the study area.

BayHunter is based on a reversible-jump Markov-chain Monte Carlo approach (Bodin and Sambridge, 2009). Starting from an initial 1D subsurface model, the algorithm iteratively perturbs the layer thicknesses, shear-wave velocities, and number of layers (Bodin et al., 2012). At each iteration, a candidate model is evaluated according to its associated acceptance probability.

For the inversion, we consider 1D models composed of 1-20 layers. Both V_S and V_P/V_S are treated as unknown parameters and constrained to vary between 2 and 5 km/s and between 1.5 and 2.1, respectively, consistent with typical values reported for the Southern Central Andes (Bohm et al., 2002; González-Vidal et al., 2018). These studies indicate V_S values between approximately 2.5 and 4 km/s over the depth range for which our results are considered reliable, which motivates the lower bound of 2 km/s adopted here. We acknowledge that shallower, near-surface material - particularly poorly welded or unconsolidated pyroclastic deposits - can exhibit V_S well below 2 km/s. However, given the frequency range of the dispersion curves used in this study, we do not consider the uppermost few hundred meters to be reliably resolved, and the search range was not extended downward to accommodate velocities in that shallow, poorly-constrained interval. As a consequence, the V_S values we report for the shallowest layers of the model

should be interpreted as an upper bound on the true velocity in that depth range. In addition, the data standard deviation is allowed to vary within the range 0.1–1 km/s in the inversion.

We perform the inversion using 10 independent Markov chains, each comprising 420,000 iterations, including 100,000 iterations for burn-in and 320,000 iterations for exploration (Fig. 6a). During the exploration phase, every 8th model is retained from each chain, yielding an initial ensemble of 40,000 models per chain. Chains whose median likelihood differs by more than 5% from that of the highest-likelihood chain are classified as outliers and excluded from further processing. The retained models from the remaining chains are then combined to construct the final posterior model ensemble, which is used to derive the 3D S-wave velocity model beneath Llaima volcano (Fig. 6b).

5. Results

Fig. 7 shows the three-dimensional spatial distribution of the S-wave velocity within the study area; we present horizontal slices at depths of 1–20 km at 1-km intervals. Although the S-wave velocity model is considered reliable to 18 km depth, it is shown to 20 km depth to provide a consistent visualization of its full extent. The velocity distribution reveals three distinct depth domains, separated at approximately 4 km and 10 km depth below the surface. Within these domains, we identify three anomalous low-velocity volumes –defined in this study as regions whose average velocity differs by

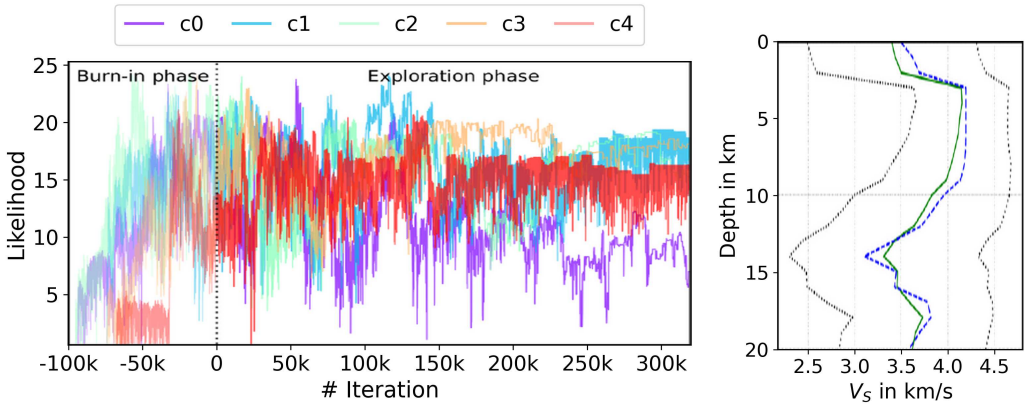

Fig. 6 Inversion results for a node located 1 km from Llaima volcano. (a) Evolution of the solution likelihood with iteration number for five independent, non-outlier chains (c0–c4). (b) Mean (green curve) and median (dashed blue curve) inverted velocity models for the same inversion node, with the minimum and maximum velocities at 1 standard deviation shown by the dashed black curves. The models are shown down to 20 km for visualization purposes; based on our sensitivity analysis, only depths down to 18 km are considered reliable

at least 5% from the mean velocity at the corresponding depth range– and no anomalous high-velocity volumes.

In addition, the reported dimensions of these anomalous bodies are restricted to the area of highest ray density, where the model resolution is sufficiently reliable. Consequently, any portions of these structures that may extend beyond this well-resolved region are not included in the reported dimensions.

The average S-wave velocity in the upper 4 km of the subsurface is 3.07 km/s. Within this depth range, the figure highlights three volumes characterized by low S-wave velocity, labeled Zone 1 ($\sim$486 km^3), Zone 2 ($\sim$273 km^3), and Zone 3 ($\sim$175 km^3) in Fig. 7. These volumes exhibit similar av-

erage velocities (2.52 km/s), corresponding to anomalies of 0.55 km/s (i.e., –17.9% relative to the average velocity at these depths).

Between 4 and 10 km depth, the average velocity increases to ∼4.03 km/s. Most volumes in this depth range exhibits values close to this average, with only minor deviations (less than 3%), which we consider negligible. Below 10 km depth, down to 18 km, our model indicates an average S-wave velocity of ∼4.2 km/s. We identify low-velocity values of ∼3.45 km/s, corresponding to anomalies of –0.75 km/s (–17.8%). This anomaly lies beneath Zone 2 at 10 km depth and extends beneath both Zone 1 and Zone 2 at 18 km depth, with a total volume of ∼1734 km^3.

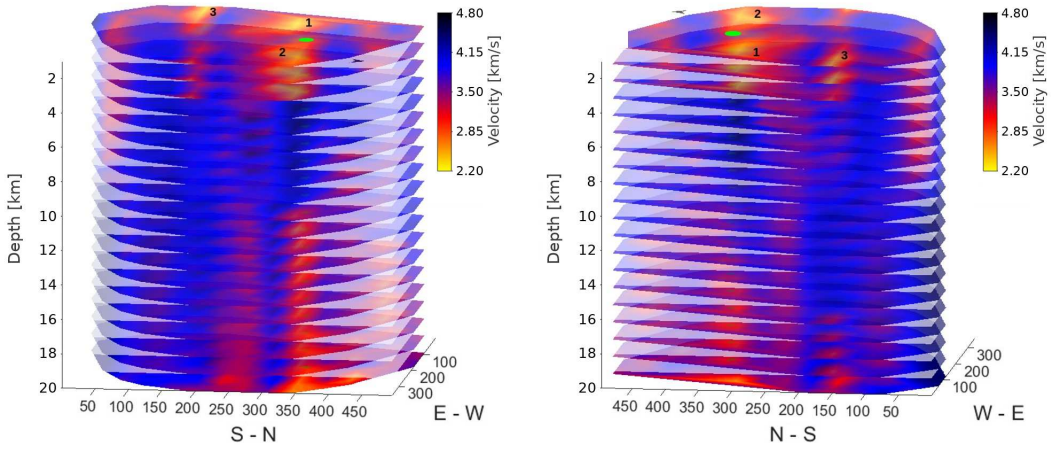

Fig. 7 Three-dimensional spatial distribution of the S-wave velocities, shown as horizontal slices from 1 to 20 km depth (shown to 20 km for visualization purposes; the model is considered reliable to 18 km depth). (Left) A view from the East and (Right) from the West. The green circle marks the location of Llaima volcano. In the horizontal plane, the coordinate $(0, 0)$ corresponds to the southwestern boundary of the study area (38.969°S,71.908°W). The horizontal scale of the map is $100\,units = 0.1°$

6. Interpretation and Discussion

Paulatto et al. (2022) analyzed a database of seismic tomography studies conducted in volcanic areas, providing statistical insights into reported methodologies, velocity variations, dimensions of anomalous structures, and inferred melt percentages. For volcanoes in subduction settings, they reported an average S-wave velocity anomaly of -25% and a median of -20%. Our results are consistent with these values, showing anomalies on the order of -18%, close to the database median. Such velocity anomalies are controlled by multiple factors, including the composition of the solid matrix, fluid content (gas and melt), temperature, pressure, porosity, permeability, viscosity, and crack density (Lees, 2007). Constraining the relative contribution of each factor in a specific volcanic setting requires a multidisciplinary approach that integrates rock physics, petrological characterization, thermal modeling, and geophysical observations (Scarpa and Gasparini, 1996; Annen et al., 2014; Giordano and Caricchi, 2022). Although further studies at Llaima are necessary to quantitatively assess the dominance of these factors, we discuss their likely influence on our results. Previous studies highlight the strong role of active tectonics at Llaima (Cembrano and Lara, 2009), as well as clear evidence of magmatic components in the subsurface (Franco et al., 2019). Together with these findings, our results suggest that both tectonic processes and the presence of melt are major contributors to the observed low-velocity anomalies. Based on these observations, we propose a structural model of the magmatic system beneath Llaima volcano.

Regarding the depth of interpretation, we note a difference in the vertical reference used here compared to previous studies at Llaima: seismic studies, including ours, report depths relative to mean station elevation, whereas geochemical studies reference depths to the base of the volcanic edifice. Based on approximate elevation values, the resulting offset is on the order of ∼250 m when compared with other seismic studies and ∼490 m when compared with geochemical studies. We consider this offset small relative to the depths discussed here and do not apply an additional shift before comparing depths across studies.

The influence of the physical controlling factors varies with depth; for instance, shallow volumes (less than 4 km depth) are more strongly affected by tectonically induced anisotropy and compositional heterogeneity related to volcanic products. At very shallow levels, the study area is characterized by abundant pyroclastic deposits. While some are consolidated, many remain poorly welded or unconsolidated, resulting in high-porosity materials (Naranjo and Moreno, 2005). In addition, Zone 3 is located in an area of near-surface fluid circulation, suggesting possible fluid saturation and potential hydrothermal alteration.

We note that the frequency range of the dispersion curves used in this study limits our depth resolution in the uppermost few hundred meters (Section 4), and consequently the velocity values obtained for the shallowest layers should be regarded as an upper bound of the true velocity. This holds independently of the physical mechanism invoked below, several of which

316 are known to reduce velocities below the lower limit of our search range (2
317 km/s) in shallow volcanic settings. Accordingly, we interpret the low-velocity
318 anomalies in Zones 1, 2, and 3 as features within the resolved portion of the
319 model, consistent with, though not a direct measurement of, the processes
320 discussed below.

321 The Liquiñe-Ofqui Fault System exerts first-order control on volcanism at
322 the latitude of Llaima (Cembrano and Lara, 2009); for reference, the surface
323 trace of its principal fault, the Liquiñe-Ofqui Main Fault, is shown in Fig. 8a.
324 Active dextral and dextral-reverse faulting has led to a highly permeable,
325 structurally damaged crust, facilitating fluid migration and the emplacement
326 of magma bodies at multiple crustal levels. As a result, volcanic structures
327 such as pyroclastic cones tend to align with the maximum stress direction
328 (NE–SW) (Lara et al., 2008). This pattern is clearly expressed at Llaima,
329 which hosts approximately 40 satellite structures. As shown in Fig. 8a and
330 supported by geological mapping (Naranjo and Moreno, 2005; Schonwalder-
331 Angel et al., 2018), the low-velocity anomalies identified as Zone 1 and Zone
332 2 spatially correlate with these satellite structures (ellipses in Fig. 8a). In
333 contrast, Zone 3 aligns with a fault structure located along the Allipén River
334 valley (UF in Fig. 8a).

335 These geological conditions, combined with fracturing associated with
336 active tectonics, are consistent with mechanisms known to reduce seismic
337 velocities (Aloisi et al., 2002; Lees, 2007; Koulakov, 2022). In Zones 1 and 2,
338 their proximity to the crater and the volcanic structures on the surface further

suggests that partial melt may also contribute to the observed anomalies. Although these processes collectively explain the low-velocity values observed across all indicated zones, additional multidisciplinary studies are required to constrain the dominant mechanisms at shallow depths. We recommend complementing the present results with V_p/V_s ratios to evaluate fluid and alteration effects, attenuation studies to assess melt and fluid content, and resistivity measurements to better distinguish rock types.

No significant velocity anomalies are observed between 4 and 10 km depth (the "transfer zone" in Fig. 9). We interpret this as reflecting the ascent pathway of magmatic components, where potential magma accumulations may be too small to be resolved at the current seismic network resolution. This interpretation supports both efficient upward migration of magma through these depths and the idea that long-lived magma storage prior to eruption occurs at shallow depths -within the upper 4 km (Ruth et al., 2016).

Our model (Fig. 9) is consistent with previous estimates of magma-storage depths beneath Llaima (De Maisonneuve et al., 2012a; Schindlbeck et al., 2014; Ruth et al., 2016; Bishop et al., 2018). Petrological constraints indicate that recent eruptions are triggered by increased gas pressure within a crystal mush located at depths of 1–4 km. When this pressure exceeds a threshold, it can lead to explosive activity (De Maisonneuve et al., 2012a; Ruth et al., 2016). Given the proximity of Zones 1 and 2 to the crater (Figs. 7 and 8), we raise the question of their role in the eruptive dynamics of the system.

The spatial relationship between low-velocity anomalies and seismicity

at Llaima provides additional insights. Both long-period events during 2009-2013 (Franco-Marín et al., 2023) and fracture events during 2010-2025 (SERNAGEOMIN, 2025) (Fig. 8a) show a preferential NW–SE alignment crossing the main edifice and extending to depths of up to 5 km, previously interpreted as subsurface stress variations caused by magma migration (Franco-Marín et al., 2023). These seismic-event locations correlate with regions of average S-wave velocity, whereas fewer than 3% occur within the low-velocity zones (some of which may even fall outside these areas given the associated location uncertainties). The scarcity of seismicity within Zones 1 and 2 suggests a more ductile rheology, characterized by increased creep and reduced viscosity and strength. This behavior supports an interpretation in which reduced velocities are linked to elevated temperature and/or increased melt fraction (Takei, 2017; Schmeling et al., 2019).

Using receiver functions, Bishop et al. (2018) identified a low-to-high velocity transition at depths of 10–15 km, interpreted as a magma accumulation zone, and a high-to-low transition near 20 km depth. We interpret the low-velocity anomaly below 10 km as indicative of partial melt (Fig. 9). This anomaly is localized near Zone 2 at 10 km depth and expands beneath both Zones 1 and 2 at $\sim$18 km depth. We infer that this deeper volume acts as a source of magma feeding the shallow reservoirs.

Our results present relevant implications for both volcanic-hazard assessment and the understanding of eruptive dynamics at Llaima volcano. Key parameters controlling volcanic behavior include reservoir depth and

dimensions, volatile content, ascent rates, conduit dynamics, and recharge frequency (Cashman et al., 2017; Scaillet et al., 2008). Although volcanic systems are highly case-dependent, shallow reservoirs are generally associated with higher eruption frequency, whereas deeper reservoirs tend to be linked to more explosive eruptions (Pallister et al., 1992; Scaillet et al., 2008; Gilbert et al., 2014).

Our findings suggest the presence of magma reservoirs at multiple crustal levels, supporting previous evidence of magma accumulation zones from deeper to shallower parts of the system. This interpretation points to active recharge of shallow reservoirs and raises further questions regarding the conditions controlling this recharge (e.g., magma volume, temperature, and viscosity), the role of magma mixing, and the mechanisms that trigger eruptions at Llaima. Additionally, our results constrain the spatial extent of potential magma reservoirs. Although these dimensions cannot be directly translated into erupted volumes, they provide an upper bound for evaluating future eruptive scenarios.

Melt fraction plays a critical role in controlling magmatic processes. The volume and temperature of ascending material determine whether heat transfer is dominated by convection or conduction (Balmforth and Rust, 2009). Melt-rich reservoirs tend to promote rapid pre-eruptive processes, whereas crystal-mush systems are associated with longer repose times (Humphreys et al., 2025). In particular, high melt fractions in the upper crust enhance interconnectivity within the mush, facilitating rapid magma transport and in-

creasing the likelihood of instability and eruption. Our results indicate shear-wave velocity anomalies of ∼18% within the interpreted reservoirs. However, translating these anomalies into quantitative melt fractions requires complex inversion frameworks that incorporate rock physics, petrology, anisotropy, and thermal structure (Paulatto et al., 2022). Therefore, our results provide not only information about the location and dimensions of magma reservoirs in the subsurface of Llaima volcano but also a foundation for future multi-disciplinary studies aimed at better constraining subsurface conditions and refining interpretations of the magmatic system.

7. Conclusions

Llaima volcano is characterized by explosive eruptions posing a high risk to the population located in its surroundings. Knowledge about the location and dimensions of its subsurface magma-accumulation volumes is fundamental for a complete understanding of the processes leading to the eruptive phenomena. Based on ambient seismic noise recorded by 49 stations from three seismic networks, we performed a tomographic inversion integrated with a Bayesian framework, allowing for a robust and data-driven characterization of the subsurface shear-wave velocity beneath Llaima volcano. We retrieved empirical Green's functions for the subsurface between every pair of stations and estimated Rayleigh-wave phase velocities. We used these velocity estimates to perform surface-wave tomography and to build a three-dimensional shear-wave velocity model down to 18 km depth.

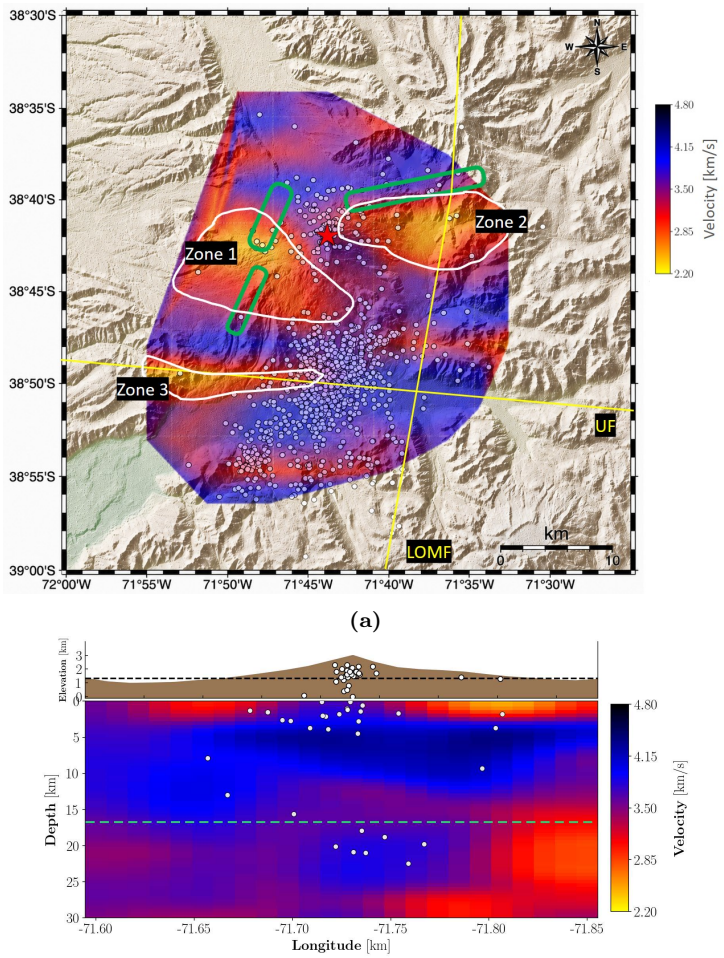

Fig. 8 (a) S-wave velocity distribution at 1 km depth over topographical map. White lines delimit the low shear-wave velocity areas -Zone 1, Zone 2 and Zone 3. Green rectangles indicate the location of satellite volcanic structures while yellow lines indicate the location of the Liquiñe-Ofqui Main Fault (LOMF) and the Unnamed Fault (UF) north the Allipén River (Naranjo and Moreno, 2005; Schonwalder-Angel et al., 2018). A star shows the location of the Llaima crater. (b) Vertical cross-section along the latitude of Llaima Crater showing the obtained S-wave velocity distribution together with topography. Note that Elevation and Depth are plotted using different scales; in this figure only, sea level is used as the vertical reference for clarity. The horizontal dashed black line indicates the average elevation of the seismic stations. The horizontal dashed green line indicates the maximum depth of interpretation; greater depths are shown only to illustrate the locations of deeper seismic sources. In both panels, circles indicate the locations of fracture seismic events (SERNAGEOMIN, 2025)

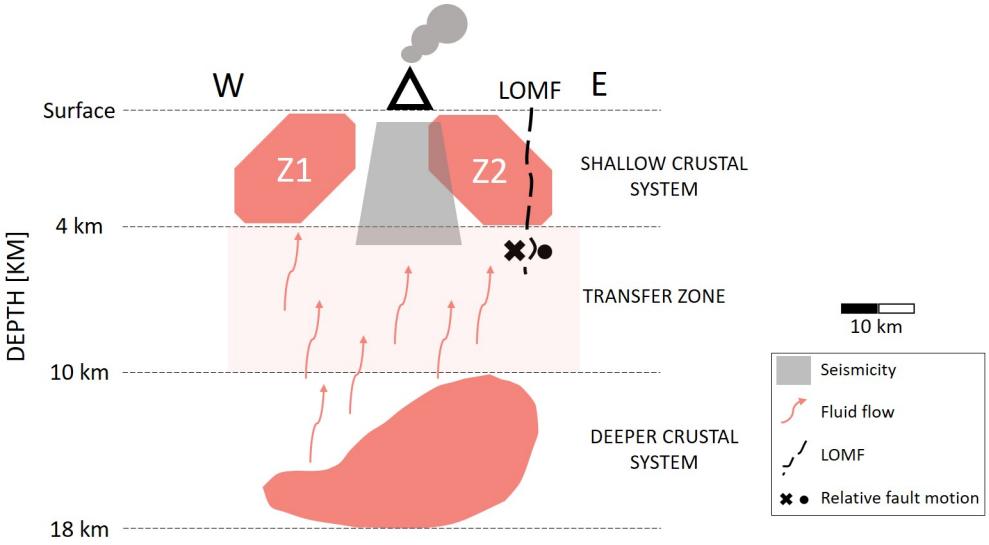

Fig. 9 Conceptual subsurface model of Llaima volcano extending to 18 km depth, along an E–W profile at the latitude of the main edifice. Shaded volumes represent low shear-wave velocity anomalies, comprising two zones (Z1—Zone 1 and Z2—Zone 2) within the shallow crustal system and one zone within the deeper crustal system. Arrows indicate the direction of fluid transport (magma and gases) within the transfer zone. The shaded seismicity area delineates the spatial distribution of local seismic events (SERNAGEOMIN, 2025). LOMF indicates the location of the Liquiñe–Ofqui Main Fault; the black cross and circle denote the dextral sense of fault motion (Schonwalder-Angel et al., 2018)

Our model supports previous results on the depth of magma-accumulation volumes, while further constraining their geometry, extent, and spatial distribution. The imaged S-wave velocity anomalies are located within two depth intervals: 1–4 km and 10–18 km. We interpreted the shallow anomalies as associated with a strong active tectonics, scoria cones, heterogeneous petrological products, and a magma-accumulation volume. In contrast, the subsurface between 4 and 10 km depth appeared to act as a transition zone without clearly resolved magma bodies. In this framework, the shallow reservoir is likely fed by a deeper source located between 10 and 18 km depth, which extends from a localized region beneath the eastern sector at 10 km depth to a broader structure underlying the entire volcanic edifice at greater depths. Together, these observations provide new evidence for a vertically segmented magmatic plumbing system beneath Llaima, characterized by distinct shallow and deep magma-storage regions connected through an intermediate transfer zone. By resolving the vertically segmented architecture of Llaima's magmatic system, our results provide a new framework for understanding eruptive dynamics, improving models of magma transport, and reinterpreting the spatial distribution of seismicity.

Data availability

Seismological data are available on the Incorporated Research Institutions for Seismology (IRIS) databases (`https://www.fdsn.org/networks/detail/XW_2015/`, `https://doi.org/10.14470/8U7569253520`) or after for-

mal request to OVDAS-SERNAGEOMIN (https://www.portaltransparencia.cl).

Code availability

The scripts required to process the data are included on Seislib python package (https://pypi.org/project/seislib/). Maps and Figures were obtained using open-source software: Global Mapping Tools (GMT, v.6.4).

References

Aloisi, M., Cocina, O., Neri, G., Orecchio, B., Privitera, E., 2002. Seismic tomography of the crust underneath the etna volcano, sicily. Physics of the Earth and Planetary Interiors 134, 139–155. doi:https://doi.org/10.1016/S0031-9201(02)00153-X.

Annen, C., Paulatto, M., Sparks, R.S.J., Minshull, T.A., Kiddle, E.J., 2014. Quantification of the intrusive magma fluxes during magma chamber growth at soufrière hills volcano (montserrat, lesser antilles). Journal of Petrology 55, 529–548. doi:10.1093/petrology/egt075.

Balmforth, N.J., Rust, A.C., 2009. Weakly nonlinear viscoplastic convection, in: Visco-plastic fluids: From theory to application, Journal of Non-Newtonian Fluid Mechanics. Elsevier, pp. 36–45. doi:https://doi.org/10.1016/j.jnnfm.2008.07.012.

Bishop, J., Lees, J., Biryol, C., Mikesell, T., Franco, L., 2018. Examining the interior of Llaima volcano with receiver functions. Journal of Volcanology and Geothermal Research , 1–9doi:https://doi.org/10.1016/j.jvolgeores.2017.11.022.

Bodin, T., Sambridge, M., 2009. Seismic tomography with the reversible jump algorithm. Geophysical Journal International 178, 1411–1436. doi:https://doi.org/10.1111/j.1365-246X.2009.04226.x.

Bodin, T., Sambridge, M., Tkalčić, H., Arroucau, P., Gallagher, K., Rawlinson, N., 2012. Transdimensional inversion of receiver functions and surface wave dispersion. Journal of geophysical research: solid earth 117. doi:https://doi.org/10.1029/2011JB008560.

Bohm, M., Lüth, S., Echtler, H., Asch, G., Bataille, K., Bruhn, C., Rietbrock, A., Wigger, P., 2002. The southern andes between 36° and 40°s latitude: seismicity and average seismic velocities. Tectonophysics 356, 275–289. doi:https://doi.org/10.1016/S0040-1951(02)00399-2.

Cashman, K.V., Sparks, R.S.J., Blundy, J.D., 2017. Vertically extensive and unstable magmatic systems: A unified view of igneous processes. Science 355, eaag3055. doi:10.1126/science.aag3055.

Cembrano, J., Lara, L.E., 2009. The link between volcanism and tectonics in the southern volcanic zone of the Chilean Andes: A review. Tectonophysics 471, 96–113. doi:https://doi.org/10.1016/j.tecto.2009.02.038.

De Maisonneuve, C.B., Dungan, M., Bachmann, O., Burgisser, A., 2012a. Insights into shallow magma storage and crystallization at volcán llaima (andean southern volcanic zone, chile). Journal of Volcanology and Geothermal Research 211, 76–91. doi:https://doi.org/10.1016/j.jvolgeores.2011.09.010.

De Maisonneuve, C.B., Dungan, M.A., Bachmann, O., Burgisser, A., 2012b. Petrological insights into shifts in eruptive styles at volcán llaima (chile). Journal of Petrology 54, 393–420. doi:10.1093/petrology/egs073.

Dreiling, J., Tilmann, F., 2019. Bayhunter-mcmc transdimensional bayesian inversion of receiver functions and surface wave dispersion. GFZ Data Services doi:https://doi.org/10.5880/GFZ.2.4.2019.001.

Dzierma, Y., Wehrmann, H., 2010. Eruption time series statistically examined: Probabilities of future eruptions at villarrica and llaima volcanoes, southern volcanic zone, chile. Journal of Volcanology and Geothermal Research 193, 82–92. doi:https://doi.org/10.1016/j.jvolgeores.2010.03.009.

Ekström, G., Tromp, J., Larson, E.W.F., 1997. Measurements and global models of surface wave propagation. Journal of Geophysical Research: Solid Earth 102, 8137–8157. doi:https://doi.org/10.1029/96JB03729.

Franco, L., Palma, J.L., Lara, L.E., Gil-Cruz, F., Cardona, C., Basualto, D., San Martín, J., 2019. Eruptive sequence and seismic sctivity of Llaima

volcano (Chile) during the 2007-2009 eruptive period: Inferences of the magmatic feeding system. Journal of Volcanology and Geothermal Research 379, 90–105. doi:https://doi.org/10.1016/j.jvolgeores.2019.04.014.

Franco-Marín, L., Lara, L.E., Basualto, D., Palma, J.L., Gil-Cruz, F., Cardona, C., Farias, C., 2023. A long time of rest at llaima volcano following the 2010 mw 8.8 maule earthquake, chile. Journal of Volcanology and Geothermal Research 440, 107858. doi:https://doi.org/10.1016/j.jvolgeores.2023.107858.

Gilbert, D., Freundt, A., Kutterolf, S., Burkert, C., 2014. Post-glacial time series of explosive eruptions and associated changes in the magma plumbing system of lonquimay volcano, south central chile. International Journal of Earth Sciences 103, 2043–2062. doi:https://doi.org/10.1007/s00531-012-0796-x.

Giordano, G., Caricchi, L., 2022. Determining the state of activity of transcrustal magmatic systems and their volcanoes. Annual Review of Earth and Planetary Sciences 50, 231–259. doi:https://doi.org/10.1146/annurev-earth-032320-084733.

Global Volcanism Program, 2026. Global volcanism program. https://volcano.si.edu. Accessed: 2026-02-09.

González-Ferrán, O., 1995. Volcanes de Chile. Instituto Geográfico Militar. ISBN 97895620200541, p. 640.

González-Vidal, D., Obermann, A., Tassara, A., Bataille, K., Lupi, M., 2018. Crustal model of the southern central andes derived from ambient seismic noise rayleigh-wave tomography. Tectonophysics 744, 215–226. doi:https://doi.org/10.1016/j.tecto.2018.07.004.

Hansen, P.C., 1999. The L-curve and its use in the numerical treatment of inverse problems. Technical University of Denmark, DTU.

Humphreys, M.C., Namur, O., Bohrson, W.A., Bouilhol, P., Cooper, G.F., Cooper, K.M., Huber, C., Lissenberg, C.J., Morgado, E., Spera, F.J., 2025. Crystal mush processes and crustal magmatism. Nature Reviews Earth & Environment 6, 401–416. doi:https://doi.org/10.1038/s43017-025-00682-x.

Koulakov, I., 2022. Seismic tomography of kamchatkan volcanoes. Russian Geology and Geophysics 63, 1207–1244. doi:10.2113/RGG20214380.

Lange, D., Cembrano, J., Sielfeld, G., 2019. Crustal Seismicity along for the Southern Andes Volcanic Zone (LOFS). URL: https://geofon.gfz.de/doi/network/3H/2014, doi:10.14470/8U7569253520.

Lara, L.E., Cembrano, J., Lavenu, A., 2008. Quaternary vertical displacement along the liquiñe-ofqui fault zone: Differential

uplift and coeval volcanism in the southern andes? International Geology Review 50, 975–993. URL: https://doi.org/10.2747/0020-6814.50.11.975, doi:10.2747/0020-6814.50.11.975, arXiv:https://doi.org/10.2747/0020-6814.50.11.975.

Lara, L.E., Flores, F., Calderón, R., Cardona, C., 2021. Chapter 17 - volcano hazards and risks in chile, in: Papale, P. (Ed.), Forecasting and Planning for Volcanic Hazards, Risks, and Disasters. Elsevier. volume 2 of *Hazards and Disasters Series*, pp. 617–633. URL: https://www.sciencedirect.com/science/article/pii/B9780128180822000172, doi:https://doi.org/10.1016/B978-0-12-818082-2.00017-2.

Lees, J.M., 2007. Seismic tomography of magmatic systems. Journal of Volcanology and Geothermal Research 167, 37–56. URL: https://www.sciencedirect.com/science/article/pii/S0377027307001965, doi:https://doi.org/10.1016/j.jvolgeores.2007.06.008. large Silicic Magma Systems.

Magrini, F., Lauro, S., Kästle, E., Boschi, L., 2022. Surface-wave tomography using seislib: a python package for multiscale seismic imaging. Geophysical Journal International 231, 1011–1030. doi:https://doi.org/10.1093/gji/ggac236.

Mikesell, T.D., 2015. Llaima volcano dataset. URL: https://www.fdsn.org/networks/detail/XW_2015/, doi:10.7914/SN/XW_2015.

Naranjo, J.A., Moreno, H., 1991. Actividad explosiva postglacial en el volcan llaima, andes del sur (38° 45's). Andean Geology 18, 69–80. URL: https://www.andeangeology.cl/index.php/revista1/article/view/2483.

Naranjo, J.A., Moreno, H., 2005. Geología del volcán Llaima, región de la Araucanía. Serie Geología Básica , 33URL: https://tiendadigital.sernageomin.cl/en/-basic-geology/942-2005geologia-del-volcan-llaima-escala-1-50000.html.

Pallister, J.S., Hoblitt, R.P., Crandell, D.R., Mullineaux, D.R., 1992. Mount st. helens a decade after the 1980 eruptions: magmatic models, chemical cycles, and a revised hazards assessment. Bulletin of Volcanology 54, 126–146. doi:https://doi.org/10.1007/BF00278003.

Paulatto, M., Hooft, E.E.E., Chrapkiewicz, K., Heath, B., Toomey, D.R., Morgan, J.V., 2022. Advances in seismic imaging of magma and crystal mush. Frontiers in Earth Science Volume 10 - 2022. doi:10.3389/feart.2022.970131.

Petit-Breuilh Sepúlveda, M.E., 2018. Desastres naturales y ocupación del territorio en Hispanoamérica. volume 70. Servicio de Publicaciones de la Universidad de Huelva. ISBN 9788417066888, p. 344.

Romero, J.E., Vergara-Pinto, F., Forte, P., Ovalle, J.T.A., Sánchez, F., 2024. The Andean Southern Volcanic Zone: a review on the legacy of the latest volcanic eruptions. Andean geology 51, 379 – 412.

URL: http://www.scielo.cl/scielo.php?script=sci_arttext&pid=S0718-71062024000200379&nrm=iso, doi:10.5027/andgeov51n2-3681.

Ruth, D.C., Cottrell, E., Cortés, J.A., Kelley, K.A., Calder, E.S., 2016. From passive degassing to violent strombolian eruption: the case of the 2008 eruption of Llaima volcano, Chile. Journal of Petrology 57, 1833–1864. doi:https://doi.org/10.1093/petrology/egw063.

Scaillet, B., Pichavant, M., Cioni, R., 2008. Upward migration of vesuvius magma chamber over the past 20,000 years. Nature 455, 216–219. doi:https://doi.org/10.1038/nature07232.

Scarpa, R., Gasparini, P., 1996. A review of volcano geophysics and volcano-monitoring methods, in: Monitoring and Mitigation of Volcano Hazards. Springer Berlin Heidelberg, pp. 3–22. doi:10.1007/978-3-642-80087-0_1.

Schindlbeck, J., Freundt, A., Kutterolf, S., 2014. Major changes in the post-glacial evolution of magmatic compositions and pre-eruptive conditions of llaima volcano, andean southern volcanic zone, chile. Bulletin of Volcanology 76, 830. doi:https://doi.org/10.1007/s00445-014-0830-x.

Schmeling, H., Marquart, G., Weinberg, R., Wallner, H., 2019. Modelling melting and melt segregation by two-phase flow: new insights into the dynamics of magmatic systems in the continental crust. Geophysical Journal International 217, 422–450. doi:10.1093/gji/ggz029.

Schonwalder-Angel, D., Cortés, J.A., Calder, E.S., 2018. The interplay of magmatism and tectonics: An example based on the satellite scoria cones at Llaima volcano, Chile. Journal of Volcanology and Geothermal Research 367, 31–45. doi:https://doi.org/10.1016/j.jvolgeores.2018.10.020.

SERNAGEOMIN, 2025. Red Nacional de Vigilancia Volcánica, Servicio Nacional de Geología y Minería, Chile. https://www.sernageomin.cl/red-nacional-de-vigilancia-volcanica/. URL: https://www.sernageomin.cl/red-nacional-de-vigilancia-volcanica/.

Stern, C., 2004. Active andean volcanism: its geologic and tectonic setting. Revista geológica de Chile 31, 161–206. doi:http://dx.doi.org/10.4067/S0716-02082004000200001.

Strollo, A., Bindi, D., Parolai, S., Jäckel, K.H., 2008. On the suitability of 1 s geophone for ambient noise measurements in the 0.1–20hz frequency range: experimental outcomes. Bulletin of Earthquake Engineering 6, 141–147. doi:10.1007/s10518-008-9061-x.

Takei, Y., 2017. Effects of partial melting on seismic velocity and attenuation: A new insight from experiments. Annual review of Earth and planetary sciences 45, 447–470. doi:https://doi.org/10.1146/annurev-earth-063016-015820.

Völker, D., Kutterolf, S., Wehrmann, H., 2011. Comparative mass balance of volcanic edifices at the southern volcanic zone of the Andes between 33°s

and 46°s. Journal of Volcanology and Geothermal Research 205, 114–129. doi:https://doi.org/10.1016/j.jvolgeores.2011.03.011.

Wassermann, J., 2012. Volcano seismology, in: New manual of seismological observatory practice 2 (NMSOP-2). Deutsches GeoForschungsZentrum GFZ, pp. 1–77. doi:10.2312/GFZ.NMSOP-2_ch13.

Zhang, S., 2018. Senskernel code. URL: https://github.com/NoiseCIEI/SensKernel.git.

Acknowledgments

The authors acknowledge support from the MAGMA project, funded by the European Research Council (Consolidator Grant No. 771143, 2018–2023), hosted at Johannes Gutenberg University Mainz, Germany. The authors particularly acknowledge the contributions of Luca de Siena and Fabrizio Magrini.

The authors also thank Jordan Bishop, Timothy J. Ronan, Rebecca Rodd, Jeffery B. Johnson, Thomas L. Otheim, and Jonathan Lees for their assistance with field data collection.

Funding

No funding was received for conducting this study.

Author information

Authors and Affiliations

Observatorio Argentino de Vigilancia Volcánica (OAVV), Servicio Geológico Minero Argentino, CONICET, Buenos Aires, Argentina

J. Augusto Casas

Centro de Investigaciones Geofísicas (CIGEOF), Universidad Nacional de La Plata, La Plata, Argentina

J. Augusto Casas, Damián Inghilterra, Gabriela Badi

Observatorio Vulcanológico de los Andes del Sur, Servicio Nacional de Geología y Minería, Temuco, Chile

Luis Franco-Marín

Norwegian Geotechnical Institute, Oslo, Norway

T. Dylan Mikesell

Department of Geoscience and Engineering, Delft University of Technology, Delft, The Netherlands Deyan Draganov

Contributions

Conceptualization: JAC, GB, TDM, LFM, DD; Software: JAC, DI; Formal analysis: JAC, DI; Resources: TDM, LFM; Writing—original draft: JAC, DI, GB; Writing—review and editing: JAC, DI, GB, TDM, LFM, DD; Supervision: GB, TDM, DD. All authors have read and agreed to the published version of the manuscript.

Ethics declarations

The authors declare no competing interests.

Supplementary Files

This is a list of supplementary files associated with this preprint. Click to download.

- CasasetalSuppMaterial.pdf